An immersed boundary method for simulating vesicle dynamics in three dimensions

Yunchang Seol [a], Wei-Fan Hu [b], Yongsam Kim [c], Ming-Chih Lai [d],∗

[a] *National Center for Theoretical Sciences, No. 1, Sec. 4, Roosevelt Road, National Taiwan University, Taipei 10617, Taiwan*
[b] *Department of Applied Mathematics, National Chung Hsing University, 145, Xingda Road, Taichung City 402, Taiwan*
[c] *Department of Mathematics, Chung-Ang University, Dongjak-Gu, Heukseok-Dong 221, Seoul 156-175, South Korea*
[d] *Center of Mathematical Modeling and Scientific Computing & Department of Applied Mathematics, National Chiao Tung University, 1001, Ta Hsueh Road, Hsinchu 300, Taiwan*

ARTICLE INFO

ABSTRACT

We extend our previous immersed boundary (IB) method for 3D axisymmetric inextensible vesicle in Navier–Stokes flows (Hu et al., 2014 [17]) to general three dimensions. Despite a similar spirit in numerical algorithms to the axisymmetric case, the fully 3D numerical implementation is much more complicated and is far from straightforward. A vesicle membrane surface is known to be incompressible and exhibits bending resistance. As in 3D axisymmetric case, instead of keeping the vesicle locally incompressible, we adopt a modified elastic tension energy to make the vesicle surface patch nearly incompressible so that solving the unknown tension (Lagrange multiplier for the incompressible constraint) can be avoided. Nevertheless, the new elastic force derived from the modified tension energy has exactly the same mathematical form as the original one except the different definitions of tension. The vesicle surface is discretized on a triangular mesh where the elastic tension and bending force are calculated on each vertex (Lagrangian marker in the IB method) of the triangulation. A series of numerical tests on the present scheme are conducted to illustrate the robustness and applicability of the method. We perform the convergence study for the immersed boundary forces and the fluid velocity field. We then study the vesicle dynamics in various flows such as quiescent, simple shear, and gravitational flows. Our numerical results show good agreements with those obtained in previous theoretical, experimental and numerical studies.

© 2016 Elsevier Inc. All rights reserved.

1. Introduction

A vesicle is a liquid droplet with a radius of about 10 µm enclosed by a phospholipid membrane suspended in an incompressible viscous fluid media. Such phospholipid membrane consists of two-layer tightly packed lipid molecules with hydrophilic heads facing the exterior and interior fluids while the hydrophobic tails hide in the middle. This bilayer membrane has the thickness about 6 nm and exhibits resistance against membrane dilation and bending. Therefore, it is quite natural to regard this membrane as an incompressible surface with mechanical functions determined by some energy functional [16]. Thus, the dynamics of vesicle in fluids can be determined by the membrane incompressibility, bending, and hydrodynamical forces. The study of vesicle dynamics in fluid flow has become an active research area in the communities

---

of soft matter physics and computational fluid mechanics in the past years. For example, understanding of vesicle behaviors in fluid flows might lead to a better knowledge of red blood cells (RBCs) in blood simply because they both share similar mechanical behaviors [33]. Certainly, it has other practical applications such as a drug-delivery vehicle for cancer therapy [40] and a micro-reactor [13] for enzymatic mRNA synthesis in bioengineering.

The interaction between the vesicle and surrounding fluid makes the dynamics rich from physical point of view. For instance, a vesicle can undergo tank-treading, tumbling, or trembling motion under shear flow, see [6] and the references therein. For the past two decades, the vesicle dynamics in general flows (particularly in shear flow) have been extensively studied by experiments [22,24,6], theories [25,32,28,11], and numerical simulations, see the detailed references below.

The numerical simulations of the vesicle problem not only involve a two-phase incompressible flow but also require to enforce an incompressibility constraint of the membrane surface, which makes the problem more challenging. The numerical methods for simulating vesicle problems in literature can be characterized by how the membrane surface is represented and how the fluid equations are solved. Based on this characterization, several methods have been developed such as boundary integral method [26,43,44,3,45,50,12], level set method [29,37,27,30,8], phase field method [9,2,30,1], particle collision method [34], immersed interface method [21,41], and immersed boundary method or front-tracking method [18,20, 48,17]; just to name a few recent ones. In all of these numerical methods, how to impose the membrane incompressibility constraint is an important issue. The surface tension in vesicle problems, which has a different physical meaning from that in general two-phase flow problems, is unknown a priori and in fact acts like Lagrange multiplier to enforce the local incompressibility along the surface. This is exactly the same role played by the pressure to enforce the fluid incompressibility in Navier–Stokes equations.

There are two different approaches to enforce the local incompressibility constraint in literature. The first one needs to discretize the whole equations first (regardless of using boundary integral, finite element, or finite difference method) and then to solve the discretized equations simultaneously for the tension and fluid variables. This approach can be explicit or semi-implicit depending on how we treat the tension force computations. There usually exists a trade-off between the time-step stability and efficiency in those algorithms simply because iterative procedures are needed. Most of the boundary integral method [45,3,50] or level set method [37,27] fall into this category. Another approach, which was used in our previous 3D axisymmetric case [17], is called a penalty idea. Instead of keeping the vesicle membrane locally incompressible, the penalty idea makes the vesicle surface patch nearly incompressible by introducing a modified elastic tension energy. This approach replaces the unknown tension by a spring-like tension depending on the surface configuration so that we can avoid solving the whole system to obtain the variable tension, which significantly simplifies the numerical algorithm. In this paper, we extend our previous immersed boundary (IB) method for simulating incompressible vesicles in 3D axisymmetric Navier–Stokes flows [17] to general three dimensions. We shall show that the new elastic force derived from the modified tension energy has exactly the same mathematical form as the original elastic force except for the different definitions of the tension. We validate this approach by performing several numerical tests in our simulations.

The rest of the paper are organized as follows. In Section 2, we present the governing equations for the vesicle problem under the immersed boundary formulation. We also provide some notions in classical differential geometry that will be used to compute the geometrical quantities of the vesicle surface mathematically and numerically. Then we introduce our approach for a nearly incompressible vesicle surface and the modified energy. The detailed numerical algorithm is described in Section 3; we first explain how to evaluate the mean curvature vector and bending force terms on a triangulated surface, then outline the complete time-stepping scheme for the algorithm, and finally discuss how to maintain the surface mesh quality during the simulations. A series of numerical tests to validate our present algorithm is given in Section 4 which is followed by conclusion and future work in Section 5.

2. Equations of motion

We consider a single incompressible vesicle $\Gamma(t)$ suspended in a three-dimensional domain Ω filled with viscous incompressible Navier–Stokes fluid. For the IB formulation in which the fluid-related quantities are represented in Eulerian manner while the vesicle-related ones are in Lagrangian manner, the governing equations can be written as follows.

$$\rho\left(\frac{\partial \mathbf{u}}{\partial t} + (\mathbf{u} \cdot \nabla)\mathbf{u}\right) = -\nabla p + \mu \Delta \mathbf{u} + \mathbf{f} \quad \text{in } \Omega, \tag{1}$$

$$\nabla \cdot \mathbf{u} = 0 \quad \text{in } \Omega, \tag{2}$$

$$\mathbf{f}(\mathbf{x}, t) = \int_{\Gamma} \mathbf{F}(r, s, t)\delta(\mathbf{x} - \mathbf{X}(r, s, t)) \, dA, \tag{3}$$

$$\frac{\partial \mathbf{X}}{\partial t}(r, s, t) = \mathbf{U}(r, s, t) = \int_{\Omega} \mathbf{u}(\mathbf{x}, t)\delta(\mathbf{x} - \mathbf{X}(r, s, t)) d\mathbf{x}, \tag{4}$$

$$\nabla_s \cdot \mathbf{U} = 0 \quad \text{on } \Gamma. \tag{5}$$

Here, we assume that the fluids inside and outside vesicle have the same density ρ and viscosity μ. Eqs. (1) and (2) are the incompressible Navier–Stokes equations with the fluid velocity $\mathbf{u}(\mathbf{x}, t)$ and the pressure $p(\mathbf{x}, t)$, where $\mathbf{x} = (x, y, z)$ is

Cartesian coordinates in Ω and t is time. The vesicle boundary is a two-dimensional surface imbedded in Ω and is denoted by $\Gamma(t) = \{\mathbf{X}(r, s, t); 0 \le r \le L_r, 0 \le s \le L_s\}$, where r and s are both Lagrangian coordinates. Notice that, in practice, it is unlikely to keep the global Lagrangian coordinates tracking the vesicle surface during the simulation so here $\mathbf{X}(r, s, t)$ is used just for the representation purpose.

In Eq. (3), the Eulerian force density $\mathbf{f}$ is a singular force term obtained by the integration of the Lagrangian force density $\mathbf{F}$ over the 2D vesicle boundary Γ while Eq. (4) simply shows that the vesicle boundary moves along with the local fluid velocity. The interactions between the Eulerian and Lagrangian descriptions are linked by the 3D Dirac delta function $\delta(\mathbf{x}) = \delta(x)\delta(y)\delta(z)$. Eq. (5), which represents the incompressibility condition of the vesicle surface, says that the surface divergence (denoted as $\nabla_s \cdot$) of the surface velocity is zero. Naturally, this incompressibility condition requires introducing a Lagrange multiplier in the form of Lagrangian force $\mathbf{F}$ which shall be described next.

A vesicle membrane (or vesicle boundary) is known to be incompressible and exhibits a resistance against bending. Thus, the membrane energy can be modeled by two parts; namely, the Helfrich-type energy E_b to resist the bending of the membrane [16], and the tension energy E_σ to enforce the incompressibility constraint [51]. So the total energy is

$$E = E_b + E_\sigma = \int_\Gamma \left(\frac{c_b}{2} H^2 + \sigma \right) dA, \tag{6}$$

where c_b is the bending rigidity, H is the surface mean curvature, and σ is the unknown tension which acts as a Lagrange multiplier to enforce the incompressibility condition in Eq. (5). By taking the variational derivative to the surface energy (6), one can derive the vesicle boundary force $\mathbf{F} = \mathbf{F}_b + \mathbf{F}_\sigma$ consisting of the bending force $\mathbf{F}_b$ and the elastic force $\mathbf{F}_\sigma$ as

$$\mathbf{F}_b = \frac{c_b}{2} \left(\Delta_s H + 2H(H^2 - K) \right) \mathbf{n}, \qquad \mathbf{F}_\sigma = \nabla_s \sigma - 2H\sigma \mathbf{n}, \tag{7}$$

where K is the Gaussian curvature of the membrane surface, $\mathbf{n}$ is the unit outward normal vector to the surface, ∇_s is the surface gradient operator, and Δ_s is the surface Laplacian (or Laplace–Beltrami) operator, see [46] for the detailed derivation.

In classical differential geometry [7], the surface gradient $\nabla_s \sigma$ of the tension σ on a surface patch $\mathbf{X}(r, s)$ can be computed as

$$\nabla_s \sigma = \frac{G\mathbf{X}_r - F\mathbf{X}_s}{EG - F^2} \sigma_r + \frac{E\mathbf{X}_s - F\mathbf{X}_r}{EG - F^2} \sigma_s, \tag{8}$$

where $E = \mathbf{X}_r \cdot \mathbf{X}_r$, $F = \mathbf{X}_r \cdot \mathbf{X}_s$, and $G = \mathbf{X}_s \cdot \mathbf{X}_s$ are the well-known coefficients of the first fundamental form of $\mathbf{X}$. Note that the subscripts r and s of a function denote the partial derivatives of the function with respect to r and s, respectively. Similarly, the surface divergence of a vector field $\mathbf{U}$ can be defined by

$$\nabla_s \cdot \mathbf{U} = \frac{G\mathbf{X}_r - F\mathbf{X}_s}{EG - F^2} \cdot \mathbf{U}_r + \frac{E\mathbf{X}_s - F\mathbf{X}_r}{EG - F^2} \cdot \mathbf{U}_s. \tag{9}$$

Noting that the local surface dilation factor is $|\mathbf{X}_r \times \mathbf{X}_s| = \sqrt{EG - F^2}$, and using the vector triple product formula $\mathbf{a} \times (\mathbf{b} \times \mathbf{c}) = (\mathbf{a} \cdot \mathbf{c})\mathbf{b} - (\mathbf{a} \cdot \mathbf{b})\mathbf{c}$, one can easily obtain the following useful relations

$$\mathbf{X}_s \times \mathbf{n} = \frac{G\mathbf{X}_r - F\mathbf{X}_s}{|\mathbf{X}_r \times \mathbf{X}_s|}, \quad \mathbf{n} \times \mathbf{X}_r = \frac{E\mathbf{X}_s - F\mathbf{X}_r}{|\mathbf{X}_r \times \mathbf{X}_s|}. \tag{10}$$

Thus, the surface gradient of the tension σ in Eq. (8) can also be immediately written as a succinct form without using the coefficients of the first fundamental form as

$$\nabla_s \sigma = \frac{(\mathbf{X}_s \times \mathbf{n})\sigma_r + (\mathbf{n} \times \mathbf{X}_r)\sigma_s}{|\mathbf{X}_r \times \mathbf{X}_s|}. \tag{11}$$

One can see later that the present computation for $\nabla_s \sigma$ is based on the discretization of Eq. (11).

2.1. Approach of nearly incompressible membrane

As in our previous 3D axisymmetric work [17], we adopt an approach of nearly incompressible membrane in order to avoid solving the unknown tension to enforce the incompressibility condition given in Eq. (5). To proceed, we start with the derivation of the relationship between the incompressibility condition and the surface dilation factor $|\mathbf{X}_r \times \mathbf{X}_s|$. The rate of change of surface dilation factor can be derived in the following:

$$\frac{\partial}{\partial t} |\mathbf{X}_r \times \mathbf{X}_s| = \frac{\mathbf{X}_r \times \mathbf{X}_s}{|\mathbf{X}_r \times \mathbf{X}_s|} \cdot (\mathbf{X}_{rt} \times \mathbf{X}_s + \mathbf{X}_r \times \mathbf{X}_{st})$$

$$= \mathbf{n} \cdot (\mathbf{X}_{rt} \times \mathbf{X}_s) + \mathbf{n} \cdot (\mathbf{X}_r \times \mathbf{X}_{st}) \quad \left(\text{since } \mathbf{n} = \frac{\mathbf{X}_r \times \mathbf{X}_s}{|\mathbf{X}_r \times \mathbf{X}_s|} \right)$$

$$= (\mathbf{X}_s \times \mathbf{n}) \cdot \mathbf{X}_{rt} + (\mathbf{n} \times \mathbf{X}_r) \cdot \mathbf{X}_{st} \quad (\text{using } (\mathbf{a} \times \mathbf{b}) \cdot \mathbf{c} = (\mathbf{b} \times \mathbf{c}) \cdot \mathbf{a})$$

$$= (\mathbf{X}_s \times \mathbf{n}) \cdot \mathbf{U}_r + (\mathbf{n} \times \mathbf{X}_r) \cdot \mathbf{U}_s \quad \text{(since } \mathbf{X}_t = \mathbf{U})$$

$$= \frac{G\mathbf{X}_r - F\mathbf{X}_s}{|\mathbf{X}_r \times \mathbf{X}_s|} \cdot \mathbf{U}_r + \frac{E\mathbf{X}_s - F\mathbf{X}_r}{|\mathbf{X}_r \times \mathbf{X}_s|} \cdot \mathbf{U}_s \quad \text{(using Eq. (10))}$$

$$= (\nabla_s \cdot \mathbf{U})|\mathbf{X}_r \times \mathbf{X}_s| \quad \text{(by Eq. (9))} . \tag{12}$$

This derivation not only reveals the expression of the surface divergence $\nabla_s \cdot \mathbf{U}$ explicitly but also shows that the condition $\nabla_s \cdot \mathbf{U} = 0$ is equivalent to the constant dilation factor over time, which is exactly what the local incompressibility means.

In our model for the vesicle membrane, we relax the incompressibility condition in Eq. (5) and replace the unknown tension σ in Eq. (7) by a spring-like elastic tension

$$\sigma = \sigma_0 \left(|\mathbf{X}_r \times \mathbf{X}_s| - |\mathbf{X}_r^0 \times \mathbf{X}_s^0| \right), \tag{13}$$

where $|\mathbf{X}_r \times \mathbf{X}_s|$ and $|\mathbf{X}_r^0 \times \mathbf{X}_s^0|$ are the local dilation factors at later and initial times, respectively. By choosing the stiffness constant σ_0 to be sufficiently large, we can keep those two local dilation factors as close as we like. However, since we allow the deviation of the dilation factor at later times from the initial one, the vesicle membrane is now nearly incompressible. The legitimacy of present nearly incompressible approach can be validated in our numerical results later. Under this nearly incompressible approach, we no longer need to solve the unknown tension numerically. By simply substituting this explicit form of σ in Eq. (13) into the second term of Eq. (7), we are able to compute the elastic force $\mathbf{F}_\sigma$ directly which simplifies numerical procedure significantly. The above elastic force $\mathbf{F}_\sigma$ can also be derived by taking the variational derivative with respect to $\mathbf{X}$ to the following elastic tension energy

$$E_\sigma(\mathbf{X}) = \frac{\sigma_0}{2} \iint \left(|\mathbf{X}_r \times \mathbf{X}_s| - |\mathbf{X}_r^0 \times \mathbf{X}_s^0| \right)^2 \, dr ds, \tag{14}$$

but we omit the detail here.

3. Numerical scheme

In this section, we describe our numerical scheme and some implementation details for solving the equations of motion presented in the previous section. Before to proceed, we perform a non-dimensionalization on those governing equations first. We use the effective radius of vesicle $R_0 = \sqrt{A/4\pi} = (3V/4\pi)^{1/3}$ as the scaling length scale, where A and V are the surface area and the enclosed volume of the vesicle, respectively. The characteristic time scale t_c can be chosen depending on different flow situations. All physical variables are scaled by the associated characteristic scales as follows:

$$\mathbf{x}^* = \frac{\mathbf{x}}{R_0}, \quad t^* = \frac{t}{t_c}, \quad \mathbf{u}^* = \frac{\mathbf{u}}{R_0/t_c}, \quad p^* = \frac{t_c^2}{\rho R_0^2} p, \quad \sigma^* = \frac{R_0^2}{c_b} \sigma.$$

After some simple calculations, the dimensionless governing equations for the vesicle dynamics (after dropping * notation) can be summarized by

$$\frac{\partial \mathbf{u}}{\partial t} + (\mathbf{u} \cdot \nabla)\mathbf{u} = -\nabla p + \frac{1}{Re}\Delta\mathbf{u} + \int_\Gamma \left(\mathbf{F}_\sigma + \frac{1}{ReCa}\mathbf{F}_b \right) \delta(\mathbf{x} - \mathbf{X}(r,s,t)) \, dA, \tag{15}$$

$$\nabla \cdot \mathbf{u} = 0, \tag{16}$$

$$\mathbf{F}_\sigma = \nabla_s \sigma - 2H\sigma\mathbf{n}, \quad \mathbf{F}_b = \frac{1}{2}\left(\Delta_s H + 2H(H^2 - K)\right)\mathbf{n}, \tag{17}$$

$$\frac{\partial \mathbf{X}}{\partial t}(r,s,t) = \int_\Omega \mathbf{u}(\mathbf{x},t)\delta(\mathbf{x} - \mathbf{X}(r,s,t)) d\mathbf{x}. \tag{18}$$

There are two dimensionless numbers; namely, the Reynolds number $Re = \rho R_0^2/\mu t_c$ and the capillary number $Ca = \mu R_0^3/c_b t_c$. As discussed before, we adopt the nearly incompressible idea in which we relax the membrane incompressibility constraint Eq. (5) and replace the unknown tension by a spring-like elastic tension σ as shown in Eq. (13). Since the elastic stiffness σ_0 is chosen sufficiently large and is adjustable, the dimensionless number in front of $\mathbf{F}_\sigma$ can be absorbed in the number σ_0. We leave the detailed study on different stiffness number in Section 4.2.

3.1. Grid layouts for Eulerian and Lagrangian variables

In order to solve the Navier–Stokes equations (1)–(2), we lay out a uniform Cartesian grid with mesh width $h = \Delta x = \Delta y = \Delta z$ in the whole computational domain Ω and define the Eulerian fluid variables on the staggered marker-and-cell (MAC) grid introduced by Harlow and Welsh [15]. In the MAC grid layout, the pressure p is defined at the cell center while
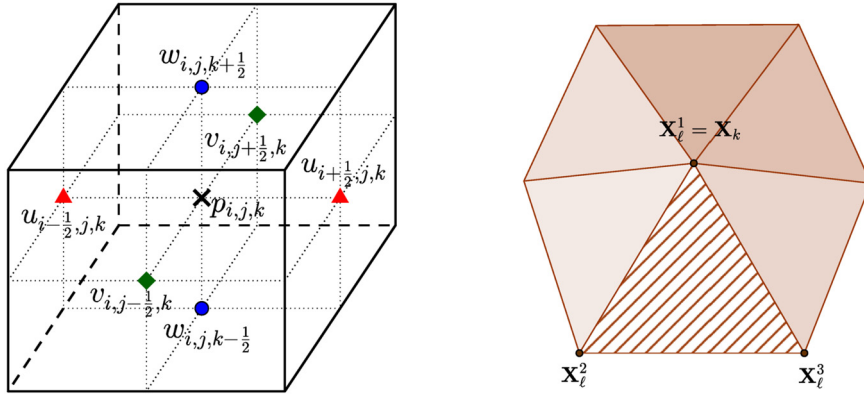
Fig. 1. Fluid variables on a staggered MAC grid in 3D (left). Triangular surface patches that share the vertex $\mathbf{X}_k$ (right).

the velocity components $\mathbf{u} = (u, v, w)$ are defined at the cell faces associated with (x, y, z) directions, see the left of Fig. 1 in detail.

For the vesicle surface Γ, we lay out a surface triangulation and define all Lagrangian variables such as mean curvature $\mathbf{H}$, elastic force $\mathbf{F}_\sigma$, and bending force $\mathbf{F}_b$ at the vertices of the triangles which are called the immersed boundary (Lagrangian) markers $\mathbf{X}$. When we choose a marker (or a vertex, say $\mathbf{X}_k$), the triangles that share the vertex make 1-ring (say $T(\mathbf{X}_k)$), see the right of Fig. 1. On a particular triangle (say the ℓ-th triangle in $T(\mathbf{X}_k)$), we denote the vertices of ℓ-th triangle in counterclockwise order viewing from outside of the surface by $\mathbf{X}_k = \mathbf{X}_\ell^1$, $\mathbf{X}_\ell^2$, and $\mathbf{X}_\ell^3$, respectively. Then the unit outward normal vector of the ℓ-th triangle can be calculated as $\mathbf{n}_\ell = \frac{(\mathbf{X}_\ell^2 - \mathbf{X}_\ell^1) \times (\mathbf{X}_\ell^3 - \mathbf{X}_\ell^1)}{|(\mathbf{X}_\ell^2 - \mathbf{X}_\ell^1) \times (\mathbf{X}_\ell^3 - \mathbf{X}_\ell^1)|}$, and the area of the ℓ-th triangle can also be easily computed as $\mathrm{d}A_\ell = |(\mathbf{X}_\ell^2 - \mathbf{X}_\ell^1) \times (\mathbf{X}_\ell^3 - \mathbf{X}_\ell^1)| / 2$.

3.2. Elastic force computation

As mentioned before, the discrete elastic force $\mathbf{F}_\sigma$ is computed at the vertices of the triangles. In the following, we shall describe how we compute the elastic tension σ, its surface gradient $\nabla_s \sigma$, and the mean curvature vector $\mathbf{H} = 2H\mathbf{n}$ at those vertex points. Once we have those values, the elastic force density at the vertex $\mathbf{X}_k$ can be computed by $\mathbf{F}_\sigma(\mathbf{X}_k) = \nabla_s \sigma(\mathbf{X}_k) - \sigma(\mathbf{X}_k)\mathbf{H}(\mathbf{X}_k)$.

In a continuous level, the physical meaning of the spring-like tension in Eq. (13) is to keep the surface patch dilation factor (thus, surface patch area by multiplying $drds$) close to the initial one. Therefore, it is quite natural to compute the tension on each triangle (say the ℓ-th triangle) by

$$\sigma_\ell = \tilde{\sigma}_0 \left(\mathrm{d}A_\ell - \mathrm{d}A_\ell^0 \right), \tag{19}$$

where formally $\tilde{\sigma}_0 = \sigma_0 / (drds)$, and $\mathrm{d}A_\ell$ and $\mathrm{d}A_\ell^0$ refer to the areas of the same triangle at two different times. Using the value of σ_ℓ on each triangle, the tension at vertex can be calculated by

$$\sigma(\mathbf{X}_k) = \sum_{\ell \in T(\mathbf{X}_k)} \sigma_\ell / 3,$$

where $1/3$ comes from the fact that a triangle consists of three different vertices. Then we can compute the surface gradient $\nabla_s \sigma$ on each triangle by

$$\nabla_s \sigma_\ell = \frac{(\mathbf{X}_\ell^3 - \mathbf{X}_\ell^1) \times \mathbf{n}_\ell}{2\,\mathrm{d}A_\ell}(\sigma_\ell^2 - \sigma_\ell^1) + \frac{\mathbf{n}_\ell \times (\mathbf{X}_\ell^2 - \mathbf{X}_\ell^1)}{2\,\mathrm{d}A_\ell}\left(\sigma_\ell^3 - \sigma_\ell^1\right), \tag{20}$$

where σ_ℓ^i ($i \in \{1, 2, 3\}$) are the values of σ at vertices $\mathbf{X}_\ell^i$ (see the vertices layout in the right of Fig. 1). The above formula is simply a direct discretization of surface gradient in Eq. (11) under triangular mesh. Once we have the surface gradient approximation on the triangles, we can estimate the same quantity at the vertex $\mathbf{X}_k$ by

$$\nabla_s \sigma(\mathbf{X}_k) = \sum_{\ell \in T(\mathbf{X}_k)} \omega_\ell \nabla_s \sigma_\ell,$$

where $\omega_\ell = \frac{\mathrm{d}A_\ell / 3}{\mathrm{d}A(\mathbf{X}_k)}$ is the corresponding area-weight for the surrounding triangle. Note that, the effective local area at the vertex $\mathbf{X}_k$ is approximated by $\mathrm{d}A(\mathbf{X}_k) = \sum_{\ell \in T(\mathbf{X}_k)} \mathrm{d}A_\ell / 3$. This kind of area-weighted approach to obtain some geometric quantities at vertex from the values of surrounding facets is quite popular in literature such as in [48,47,3,12].

As for the mean curvature vector, we adopt the same formula used in the 3D foam paper by Kim et al. [19]. That is, the mean curvature vector $\mathbf{H} = 2H\mathbf{n}$ at each vertex $\mathbf{X}_k$ can be computed by

$$\mathbf{H}(\mathbf{X}_k) = \frac{1}{2\,dA(\mathbf{X}_k)} \sum_{\ell \in T(\mathbf{X}_k)} \mathbf{n}_\ell \times \left(\mathbf{X}_\ell^3 - \mathbf{X}_\ell^2 \right), \tag{21}$$

where $\mathbf{X}_\ell^1 = \mathbf{X}_k$ and $\mathbf{X}_\ell^i$ for $i \in \{2, 3\}$ have the same geometric locations as illustrated in the right of Fig. 1. Surprisingly, the mean curvature obtained by above formula is equivalent to the well-known cotangent formula in Meyer et al. [31]. We leave this equivalence derivation for both formulas in Appendix A. One should also mention that, the above formula for mean curvature vector can be regarded as a discrete version of $\int_S 2H\mathbf{n}\,dA = \oint_{\partial S} \mathbf{n} \times d\mathbf{X}$ over a smooth surface patch S [42].

3.3. Bending force computation

In order to compute the bending force $\mathbf{F}_b(\mathbf{X}_k)$ at the vertex $\mathbf{X}_k$, we follow the idea used in [47]. To proceed, we begin with the discrete version of bending energy in Eq. (6) as

$$E_b[\mathbf{X}] = \frac{1}{8} \sum_{k=1}^{N_v} |\mathbf{H}(\mathbf{X}_k)|^2 \, dA(\mathbf{X}_k), \tag{22}$$

where $\mathbf{H} = 2H\mathbf{n}$ is the mean curvature vector as before and N_v is the total number of vertices in the surface triangulation. Substituting the mean curvature vector formula of Eq. (21) into (22), Wu et al. [47] derived the following discrete bending force acting at the vertex $\mathbf{X}_k$,

$$\mathbf{F}_b(\mathbf{X}_k)dA(\mathbf{X}_k) = \frac{1}{8} \sum_{\ell \in T(\mathbf{X}_k)} \left((H_\ell - \mathbf{n}_\ell \cdot \mathbf{C}_\ell)\left(\frac{1}{2}\mathbf{n}_\ell \times \mathbf{E}_\ell^k\right) + \frac{1}{2}\mathbf{C}_\ell \times \mathbf{E}_\ell^k + \mathbf{n}_\ell \times \mathbf{h}_\ell^k \right), \tag{23}$$

where

$$H_\ell = \frac{1}{3} \sum_{p \in V(\ell)} |\mathbf{H}(\mathbf{X}_p)|^2, \quad \mathbf{C}_\ell = \frac{1}{dA_\ell} \sum_{p \in V(\ell)} \mathbf{E}_\ell^p \times \mathbf{H}(\mathbf{X}_p),$$

$$\mathbf{E}_\ell^k = \mathbf{X}_\ell^3 - \mathbf{X}_\ell^2, \quad \mathbf{h}_\ell^k = \mathbf{H}(\mathbf{X}_\ell^3) - \mathbf{H}(\mathbf{X}_\ell^2). \tag{24}$$

Note that, as usual, $\mathbf{X}_\ell^i$ for $i \in \{2, 3\}$ are ordered in a counterclockwise direction (viewing from outside) by fixing $\mathbf{X}_\ell^1 = \mathbf{X}_k$ to calculate $\mathbf{E}_\ell^k$ and $\mathbf{h}_\ell^k$ in Eq. (24).

3.4. Time-stepping scheme

Once we know how to represent the vesicle surface and how to compute the elastic tension and the bending force on the triangular mesh, the time integration of our scheme completely follows the traditional IB framework [35]. Let us denote the time step size by Δt and the superscript n as the time step index. At the beginning of each time step n, the vesicle configuration represented by the Lagrangian markers $\mathbf{X}_k^n$ (the vertices of surface triangular mesh) and the fluid velocity $\mathbf{u}^n$ on Eulerian grid are both given. So the numerical procedure of the IB method to obtain $\mathbf{u}^{n+1}$ and $\mathbf{X}_k^{n+1}$ can be performed as follows.

1. Compute the Lagrangian boundary force at the Lagrangian markers by

$$\mathbf{F}(\mathbf{X}_k^n)dA(\mathbf{X}_k^n) = \mathbf{F}_\sigma(\mathbf{X}_k^n)dA(\mathbf{X}_k^n) + \frac{1}{ReCa}\mathbf{F}_b(\mathbf{X}_k^n)dA(\mathbf{X}_k^n) \tag{25}$$

   where the elastic tension force $\mathbf{F}_\sigma$ and the bending force $\mathbf{F}_b$ are computed using the formulas described above.
2. Spread the Lagrangian boundary force into the Eulerian grid using the smoothed Dirac delta function δ_h as

$$\mathbf{f}^n(\mathbf{x}) = \sum_{k=1}^{N_v} \mathbf{F}(\mathbf{X}_k^n)\, dA(\mathbf{X}_k^n)\delta_h\left(\mathbf{x} - \mathbf{X}_k^n\right), \tag{26}$$

   where $\mathbf{x} = (x, y, z)$ is the fluid mesh point. For $\delta_h(\mathbf{x}) = \frac{1}{h^3}\phi\left(\frac{x}{h}\right)\phi\left(\frac{y}{h}\right)\phi\left(\frac{z}{h}\right)$, we employ

$$\phi(r) = \begin{cases} \frac{1}{8}\left(3 - 2|r| + \sqrt{1 + 4|r| - 4r^2}\right), & \text{if } |r| \leq 1, \\ \frac{1}{8}\left(5 - 2|r| - \sqrt{-7 + 12|r| - 4r^2}\right), & \text{if } 1 < |r| \leq 2, \\ 0, & \text{otherwise.} \end{cases} \tag{27}$$
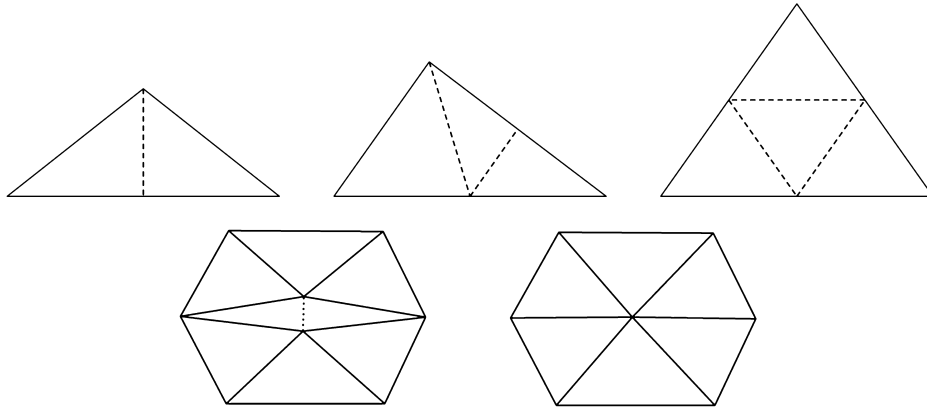
Fig. 2. Re-meshing triangulation by edge addition (top) and deletion (bottom).

3. Solve the Navier–Stokes equations. This can be done by the following backward second-order projection method [14] in which the nonlinear term is approximated by the Adams–Bashforth scheme.

$$\frac{3\mathbf{u}^* - 4\mathbf{u}^n + \mathbf{u}^{n-1}}{2\Delta t} + 2\left(\mathbf{u}^n \cdot \nabla_h\right)\mathbf{u}^n - \left(\mathbf{u}^{n-1} \cdot \nabla_h\right)\mathbf{u}^{n-1} = -\nabla_h p^n + \frac{1}{Re}\Delta_h \mathbf{u}^* + \mathbf{f}^n, \tag{28}$$

$$\Delta_h p^* = \frac{3}{2\Delta t}\nabla_h \cdot \mathbf{u}^*, \quad \frac{\partial p^*}{\partial \mathbf{n}} = 0 \text{ on } \partial\Omega, \quad \mathbf{u}^* = \mathbf{u}^{n+1} \text{ on } \partial\Omega,$$

$$\mathbf{u}^{n+1} = \mathbf{u}^* - \frac{2\Delta t}{3}\nabla_h p^*,$$

$$\nabla_h p^{n+1} = \nabla_h p^* + \nabla_h p^n - \frac{2\Delta t}{3Re}\Delta_h(\nabla_h p^*),$$

where ∇_h, $\nabla_h\cdot$, and Δ_h are the second-order central difference operators which approximate the gradient, divergence, and Laplace operator, respectively, under staggered MAC grid setting. For the nonlinear terms, the skew-symmetric form is applied as $(\mathbf{u} \cdot \nabla_h)\mathbf{u} = \frac{1}{2}(\mathbf{u} \cdot \nabla_h)\mathbf{u} + \frac{1}{2}\nabla_h(\mathbf{uu})$. One can see that the most time-consuming part in this step is to solve one Poisson equation for the pressure and three modified Helmholtz equations for the velocity field. Fortunately, these elliptic solvers can be implemented efficiently using Fast Fourier Transform (FFT).

4. Interpolate the new velocity from the Eulerian fluid points to the Lagrangian markers and then advance the markers to new positions by using

$$\mathbf{X}_k^{n+1} = \mathbf{X}_k^n + \Delta t \sum_{\mathbf{x}} \mathbf{u}^{n+1}(\mathbf{x})\delta_h(\mathbf{x} - \mathbf{X}_k^n)h^3.$$

3.5. The maintenance of triangular mesh quality

As mentioned before, we use triangular mesh to track the shape of the vesicle. To make an initial triangulation of the surface, we start by producing an icosahedron (20 triangles) on a unit sphere and then divide each triangle into 4 smaller triangles by connecting the midpoints of all edges. We then project all the new vertex points onto the unit sphere. This refinement-projection procedure is continued until proper resolution is achieved on the unit sphere. Then the initial configuration of various types of a vesicle can be constructed by applying a given function in spherical coordinates of (θ, ϕ), where $(\theta, \phi) \in [0, 2\pi] \times [0, \pi]$.

Since the vesicle surface might deform severely during the numerical simulations in dynamic flow, we apply a proper re-meshing technique to the triangular mesh to maintain the grid resolution over the surface. If the triangular mesh is too coarse, there could be some volume leakage through the boundary surface, and if it is too fine, a severe time step constraint for numerical stability could be occurred. We maintain proper resolution of the triangular mesh by simply adding or deleting marker points (and thus the triangles) as needed, in the following way.

At each time step, we scan the length of three edges for each triangle and make sure that each edge-length is between $L_{max} = 0.5h$ and $L_{min} = 0.24h$, where h is the spatial mesh width. If the length of an edge is larger than L_{max}, we add a new marker in the middle of that edge and then create more new triangles as illustrated in the upper panel of Fig. 2. We remark that the sum of area of all triangles through this refinement process is equal to the area of the original configuration. Meanwhile, if the length of an edge is less than L_{min}, we delete this edge and replace the two end points of the edge by a point located in halfway between them, see the bottom panel of Fig. 2. This process deletes two triangles which previously share the same edge. This strategy for re-meshing was applied to the numerical simulations for 3D foam dynamics in [19].
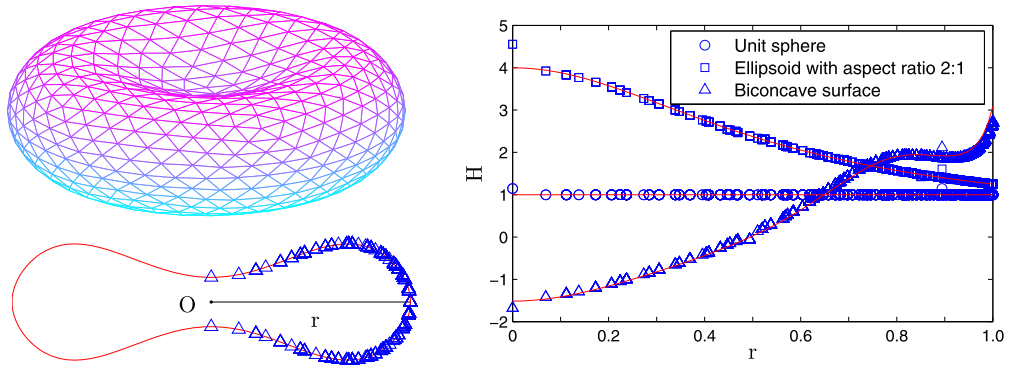
Fig. 3. Left: A triangulated biconcave surface and its cross-sectional view. Right: The comparison of mean curvature between numerical values (symbols) and exact values (solid lines) for three different surfaces. Here, the number of vertices is $N_v = 2562$ corresponding to 5120 triangles used.

If we re-mesh the triangulation of a vesicle surface at some time step through the addition or deletion of an edge, the area of some triangles would change accordingly, see Fig. 2. This certainly makes the entire numerical algorithm more complex since we adopt the nearly incompressible approach of a vesicle which uses the area difference of the triangle at later and initial times. To overcome this difficulty, when a re-meshing of the vesicle surface occurs at time t, we also apply the same re-meshing procedure to the initial surface so that a one-to-one mapping continues to exist between dA_ℓ and dA_ℓ^0 in Eq. (19).

4. Numerical results

We perform a series of numerical tests for three-dimensional vesicle simulations in fluid flows. We begin by checking the rate of convergence of the developed scheme for the computation of the mean curvature, bending force, fluid variables, and vesicle configuration. Then, we choose different stiffness coefficient $\bar{\sigma}_0$ to study its effect on the nearly incompressibility by comparing local and global surface areas. As applications, we simulate the dynamics of a suspended vesicle in quiescent, simple shear, and gravitational flows. Throughout this paper, we choose the effective radius $R_0 = 1$, the Reynolds number $Re = 1$, the capillary number $Ca = 50$, and the grid size 128^3, unless otherwise stated. The number of triangles used for an initial vesicle surface is chosen either 81920 or 327680 with the corresponding number of vertices 40962 or 163842 so that the volume leakage error is less than 1% for all simulations we have performed. Because of the vesicle deformation under dynamic flows, the redistribution of triangular mesh points described in the previous section is applied to maintain a proper resolution of a discretized vesicle. For a given initial vesicle shape, another dimensionless number named the reduced volume is defined as $\nu = \frac{3V}{4\pi (A/4\pi)^{3/2}}$ where A and V are the surface area and the enclosed volume of the vesicle, respectively. This number ν represents the volume ratio between the vesicle and the sphere with the same surface area.

4.1. Accuracy check for mean curvature and bending force

As the first test, we check the accuracy of the numerical schemes in Eqs. (21) and (23) for computing the mean curvature and the bending force, respectively. Here, we consider the following three different surfaces described in spherical parametric coordinates $(\theta, \phi) \in [0, 2\pi] \times [0, \pi]$ for which the mean curvature and other geometrical quantities in the formula for the bending force can be computed analytically.

1. Unit sphere: $\mathbf{X}(\theta, \phi) = (\cos\theta \sin\phi, \sin\theta \sin\phi, \cos\phi)$;
2. Ellipsoid: $\mathbf{X}(\theta, \phi) = (0.5 \cos\theta \sin\phi, 0.5 \sin\theta \sin\phi, \cos\phi)$;
3. Biconcave surface: $\mathbf{X}(\theta, \phi) = \left(\cos\theta \sin\phi, \sin\theta \sin\phi, (0.1242 + 0.8012 \sin^2\phi - 0.4492 \sin^4\phi)\cos\phi\right)$.

We draw the biconcave surface together with its triangular mesh in the upper-left panel of Fig. 3. In order to compare the mean curvature H at the vertices on the surface, we project the vertices onto the xy-plane and calculate the normalized distance r from the projected vertices to the origin O. For the biconcave surface, the symbols in the lower-left panel of Fig. 3 indicate the projected vertices. In the right panel, we show the point-wise values of the mean curvature with respect to the distance r for all the three different surfaces. The symbols represent the numerical values while the solid lines represent the exact values of the mean curvatures. One can see that the numerical values for the mean curvature match with the exact values quite well except at two points with $r \approx 0, 0.9$. We attribute this discrepancy to the defect of current triangulation, since these two points have only five neighboring triangles rather than six.

Even though the point-wise values of the computational mean curvature can behave not well at some vertices, as we can see from the left panel of Fig. 4, the L^2 errors for the mean curvature computation behave like first-order convergence
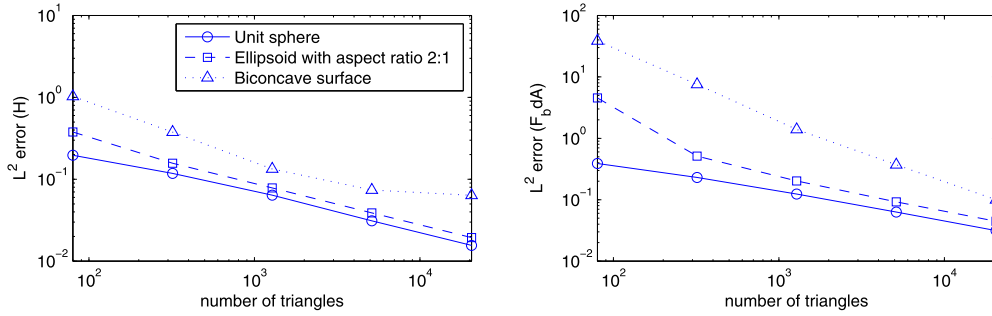
Fig. 4. The L^2 errors for the mean curvature H (left) and the bending force $\mathbf{F}_b \, dA$ (right) as functions of the number of triangles.

under the current triangulation as we increase the number of triangles. (The L^2 error of some function ψ is calculated as $\sqrt{\sum_{k=1}^{N_v} |\psi^e(\mathbf{X}_k) - \psi(\mathbf{X}_k)|^2 \, dA(\mathbf{X}_k)}$, where $\psi^e(\mathbf{X}_k)$ is the exact value and $\psi(\mathbf{X}_k)$ is the computed value. For a vector-valued function, the absolute value should be replaced by the vector norm.) We also show the L^2 errors for the bending force $\mathbf{F}_b \, dA$ in the right panel of Fig. 4. It is important to mention that, instead of studying the convergence of $\mathbf{F}_b$, we study the convergence of $\mathbf{F}_b \, dA$. This is simply because the latter one is the immersed boundary force used in Eq. (25). Again, one can see that the bending force computation still behaves like first-order convergence as we increase the number of triangles.

We should make a remark that, for general unstructured surface triangulations, the above computational values for mean curvature or bending force may not converge at all. In order to have the point-wise convergence for the mean curvature, one should construct at least a local quadratic surface at each vertex to estimate those geometric quantities [48]. However, that would make our code implementations more complicated and we leave a further improvement for computations of those geometrical quantities to future work.

4.2. Study on different stiffness parameter $\tilde{\sigma}_0$

In the usage of nearly incompressible approach introduced in Section 2.1, we should choose the stiffness parameter $\tilde{\sigma}_0$ in Eq. (19) large enough to keep the vesicle nearly incompressible. We here test three different values of $\tilde{\sigma}_0 = 6 \times 10^4$, 6×10^5, 6×10^6 to see how this change affects the local and global preservations of surface area. We put an oblate vesicle with the initial shape as

$$\mathbf{X}(\theta, \phi) = (\cos\theta \sin\phi, \sin\theta \sin\phi, \cos\phi/3.5) \tag{29}$$

in a quiescent flow of which the reduced volume is around $\nu = 0.643$. The computational domain is chosen as $\Omega = [-2, 2]^3$, and the grid number $N = 128$ is used for all spatial directions so the mesh width is $h = 1/32$. The number of triangles used in the initial vesicle surface is about 81920 with 40962 number of vertices. The time step size is chosen as $\Delta t = h/16$.

Fig. 5 shows four time evolutionary plots; namely (a) the maximum relative error of the local surface area $\|(dA^t(\mathbf{X}) - dA^0(\mathbf{X}))/dA^0(\mathbf{X})\|_\infty$, (b) the relative error of the global surface area $|A^t - A^0|/A^0$, (c) the relative error of the global volume $|V^t - V^0|/V^0$, and (d) the total energy. One can see from Fig. 5 (a) and (b) that the local and global errors of the surface area decrease as the elastic stiffness $\tilde{\sigma}_0$ increases. More precisely, when the cases of stiffness parameter $\tilde{\sigma}_0 = 6 \times 10^5$ and 6×10^6, the maximum relative errors of the local surface area are about 1% while the relative errors of the global surface area are less than 0.1% and 0.01%, respectively. It is important to mention that the errors shown in Fig. 5 (a) are in the maximum norm meaning that all the triangular elements in our discretization satisfy the area dilation or compression within 1% as time up to $t = 40$ which shows the legitimacy of present nearly incompressible approach. It is also interesting to mention that the global error decreases from the order of 10^{-2} to the order of 10^{-4} in the factor of $1/10$ as we increase $\tilde{\sigma}_0$ by a factor of 10. Of course, the maintenance of good mesh quality as described in Section 3.5 has to be adopted from time to time.

Fig. 5 (c) shows that the relative error of the global volume of the vesicle also decreases after some time as the elastic stiffness increases. Since the stiffness parameter $\tilde{\sigma}_0$ is adjustable, the readers might wonder whether different $\tilde{\sigma}_0$ cause different flow behaviors. In Fig. 5 (d), we can see that all three different $\tilde{\sigma}_0$, the total energy are almost in the same magnitude up to time $t = 40$. In other words, even we use different stiffness parameter $\tilde{\sigma}_0$, the energy contributed to the fluid system are almost the same. Although it is not shown here, the vesicle shape dynamics for those three cases are quite similar.

4.3. Study on vesicle configuration and fluid velocity

We here perform the convergence study for the present numerical algorithm. Again, we put an oblate vesicle with the same shape as in the previous subsection in quiescent flow initially. The computational domain is the same as before and we
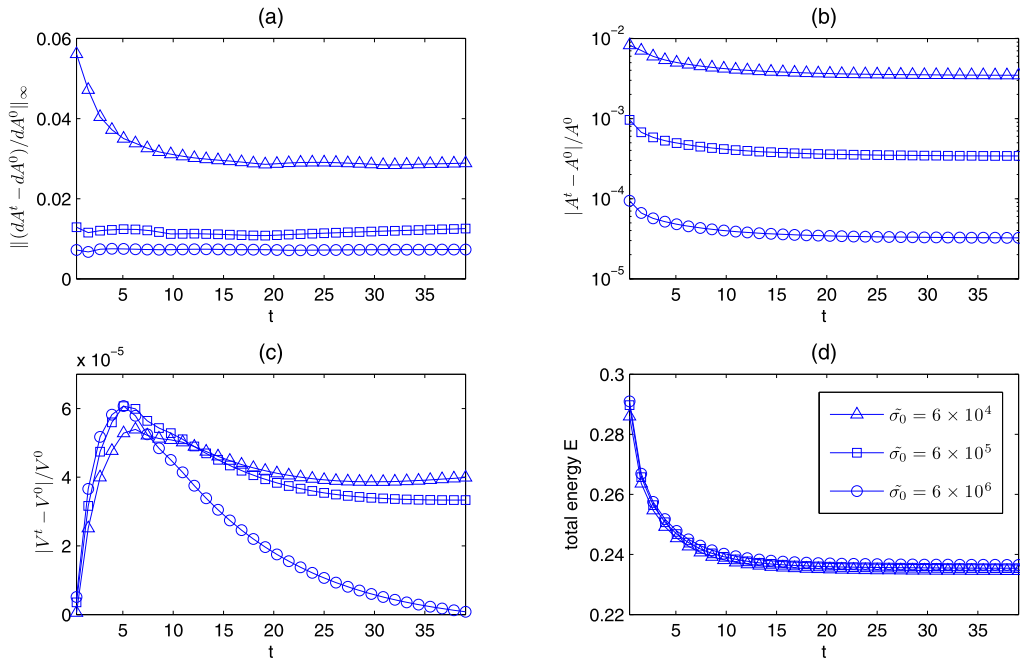
Fig. 5. The comparison for three different stiffness parameters: $\tilde{\sigma}_0 = 6 \times 10^4$ ($\triangle$), 6×10^5 ($\square$), and 6×10^6 ($\bigcirc$). (a) The maximum relative error of the local surface area; (b) the relative error of the global surface area; (c) the relative error of the global volume; (d) the total energy.
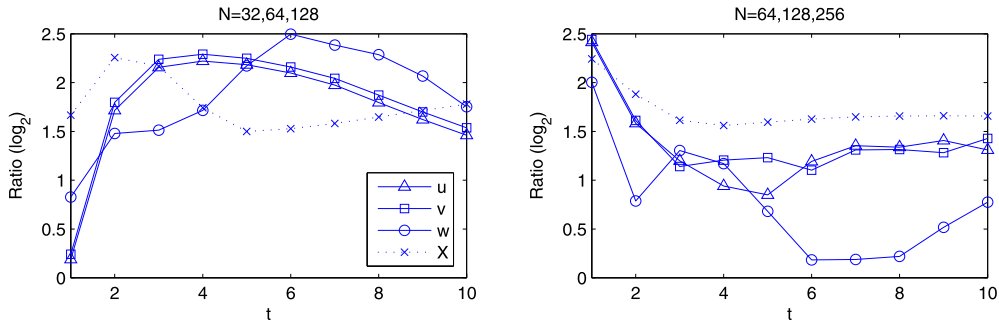
Fig. 6. The ratios of convergence for the fluid velocity (u, v, w) and the vesicle configuration **X**. Left: $N = 32$; Right: $N = 64$.

choose four different Cartesian grid sizes $N = 32, 64, 128, 256$ to study the convergence. For the vesicle surface triangulation, as we double the grid size N, we need to halve all the edges of the triangles so that the number of triangles used must be increased by a factor of four correspondingly. (For the case of $N = 32$, we use 5120 number of triangles which corresponds to 2562 number of vertices.) To be consistent, we also need to increase the stiffness parameter by a factor of four as we double the grid size, that is $\tilde{\sigma}_0 = (N/32)^2 \times 10^4$. The time step size is $\Delta t = h/8$.

Fig. 6 shows the rate of convergence for the velocity components $\mathbf{u} = (u, v, w)$ and the vesicle configuration X at some different times up to $t = 10$. Since the analytic solution is not known, we estimate the error on each grid by using the numerical solution in the next finer grid as the reference solution. In this case, for the numerical value of the x-component of the velocity u_N with the grid size N, the convergent ratio can be computed using the two successive errors as $ratio = \log_2(\|u_N - u_{2N}\|_\infty / \|u_{2N} - u_{4N}\|_\infty)$. (The ratios for the velocity components v, w and the vesicle configuration **X** are defined similarly.) One can see from Fig. 6 that the average ratio is around one, which indicates that our numerical method is roughly first-order accurate. This confirms that the IB method is first-order accurate in general. It is also interesting to mention that the velocity components u and v have pretty similar convergence behaviors due to the axis-symmetric property of the vesicle surface in the present 3D simulations.

4.4. A suspended vesicle in quiescent flow

We choose a suspended vesicle with three different initial shapes and study their equilibrium in quiescent flow. The initial shapes of the suspended vesicle are the following:
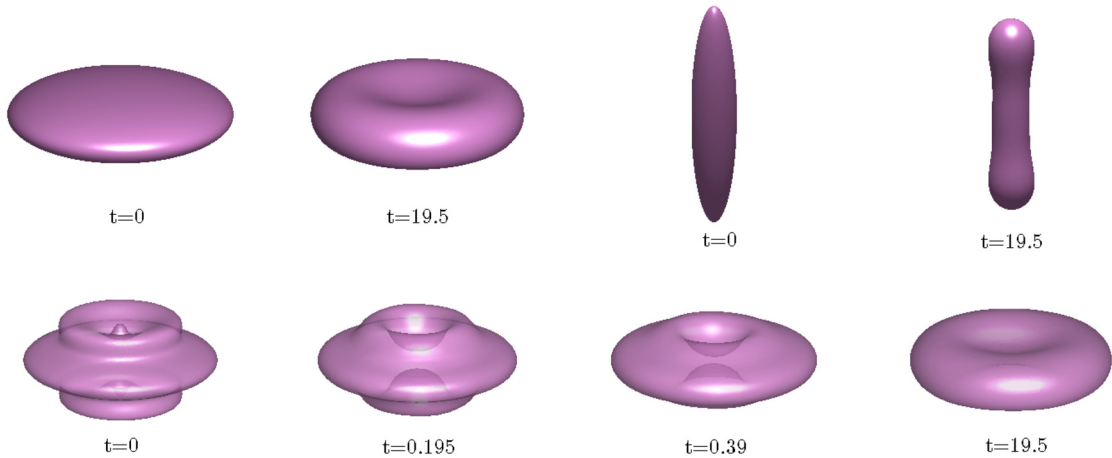
Fig. 7. Suspended vesicles in quiescent flow. Oblate vesicle (two upper-left panels); Prolate vesicle (two upper-right panels); Oscillatory vesicle (lower panels).

- Oblate surface: $\mathbf{X}(\theta, \phi) = (\cos\theta \sin\phi, \sin\theta \sin\phi, \cos\phi/3.5)$
- Prolate surface: $\mathbf{X}(\theta, \phi) = (0.2\cos\theta \sin\phi, 0.2\sin\theta \sin\phi, \cos\phi)$
- Oscillatory surface [44]: $\mathbf{X}(\theta, \phi) = \left(\frac{3}{20}r(\phi)\cos\theta \sin\phi, \frac{3}{20}r(\phi)\sin\theta \sin\phi, \frac{3}{25}r(\phi)\cos\phi\right)$, where $r(\phi) = \sqrt{\cos^2\phi + 9\sin^2\phi + \cos^2(4\phi)}$.

These vesicles have approximately the reduced volume $\nu = 0.64$, 0.63, and 0.60 correspondingly. The computational setup uses $\Omega = [-2, 2]^3$, $\tilde{\sigma}_0 = 6 \times 10^5$, and $\Delta t = h/16$. In Fig. 7, the two upper-left panels show the oblate vesicle at two different times ($t = 0$ and $t = 19.5$) where the latter one is in equilibrium. The equilibrium shape turns out to be a biconcave one which is a typical shape of RBCs. For the prolate vesicle in the two upper-right panels, the equilibrium shape turns to be a dumbbell one. For the oscillatory vesicle in the lower panel, the transition is more complicated so we provide four snapshots at four different times. One can see that the equilibrium shape also becomes a typical biconcave one which is in good agreement with those obtained in literature [44,17] despite the fact that the present simulations are fully 3D. The present results show not only the numerical stability of our scheme but also a good preservation of the symmetric structure.

4.5. A vesicle in shear flow

We simulate the dynamics of a prolate vesicle in a simple shear flow $\mathbf{u} = (z, 0, 0)$, see the schematic view of the problem setup in Fig. 8. It is well-known that there are three different flow regimes; namely, (1) a stationary tank-treading (TT) regime where the vesicle exhibits a tank-treading motion with no change of its shape in time, (2) a tumbling (TB) regime where the vesicle tumbles like a rigid body motion, and (3) a trembling (TR) regime where the major axis of the vesicle oscillates about the shear flow direction. It has been well studied in literature (see [6]) that the above three regimes can be fully characterized by the non-dimensional shear rate χ (equals to the capillary number Ca in Eq. (15) when the time scale t_c is chosen as the inverse of the shear rate), the viscosity contrast λ (the viscosity ratio between the interior and exterior fluids), and the reduced volume ν. Throughout this subsection, we use a larger computational domain $\Omega = [-3, 3]^3$ and a smaller Reynolds number $Re = 10^{-3} \ll 1$ so that we can compare our present numerical results against with the theoretical and other numerical results in Stokes regime [26]. The mesh width and the time step size are chosen as $h = 6/128$ and $\Delta t = h/64$ for these simulations. Here, we restrict our flow regime to be TT by choosing the viscosity contrast $\lambda = 1$ and TB by choosing $\lambda = 40$.

In the TT regime, we investigate the dependence of the tank-treading motion of the vesicle on the non-dimensional shear rate χ and the reduced volume ν. The initial vesicle is chosen as a prolate shape as shown in the previous subsection with five different reduced volume $\nu = 0.8$, 0.85, 0.9, 0.95, and 0.975 by keeping the effective radius $R_0 = 1$ fixed but adjusting the aspect ratio. As the shear flow turns on, the vesicle aligns with the flow direction so that a stationary tank-treading (TT) motion occurs while the vesicle shape does not change in time, see the bottom panels of Fig. 8. This feature discriminates incompressible vesicle from liquid droplet that elongates its shape as the linear shear rate increases [36]. The inclination angle is defined as the angle between the x-axis and the major axis L of a vesicle projected onto the xz-plane, see Fig. 8. This tank-treading motion can be characterized by the inclination angle θ, and the scaled tank-treading frequency ω. Here, the tank-treading frequency ω can be computed using the formula $\omega = \frac{1}{N_v}\sum_{i=1}^{N_v} \frac{|\mathbf{r} \times \mathbf{v}|}{|\mathbf{r}|^2}$, where $\mathbf{r}$ and $\mathbf{v}$ are the position and velocity of the vertices projected on the xz-plane, respectively. Fig. 9 shows the tank-treading inclination angle (left) and the scaled tank-treading frequency (right) versus the reduced volume for three different dimensionless shear rates: $\chi = 1$, 10, and 100. As in [26], we can conclude that both the inclination angle θ and the scaled tank-treading frequency ω are

Fig. 8. The simulation setup of a vesicle motion in a shear flow (top) and the tank-treading motion of a vesicle with $\nu = 0.8$ and $\lambda = 1$ in a shear flow with $\chi = 100$ (bottom).
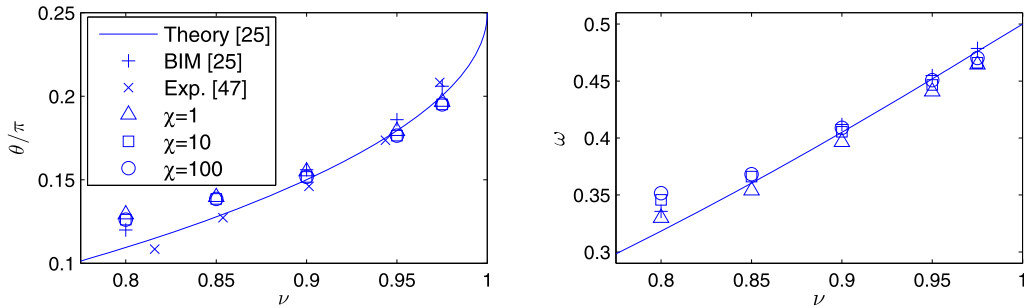
Fig. 9. The plot of the inclination angle (left) and the scaled tank-treading frequency (right) as functions of reduced volume ν for different dimensionless shear rate $\chi = 1, 10, 100$. In the left panel, the comparisons are made against with theoretical and numerical results (denoted by BIM) in [26] for $\chi = 10$, and the experiment in [49]. No tank-treading frequency results are available in [49].

independent of the shear rate χ, and the latter one seems to be almost linearly proportional to shear rate. However, both above quantities are highly dependent on the reduced volume. Furthermore, we also put the inclination angles obtained from theoretical and numerical studies (by the boundary integral method) in [26] ($\chi = 10$), and the experimental results obtained in [49] into the figure. One can see that our present results agree well with those obtained in theory and experiment especially when the reduced volume is greater than 0.9 and certainly match well with the numerical study in [26] both for the inclination angle and the tank-treading frequency.

As mentioned earlier, when the viscosity contrast λ is above a critical threshold, the vesicle under shear flow will turn the tank-treading to tumbling motion. Here, we use the same setup as previous TT case except the viscosity contrast is chosen as $\lambda = 40$. The numerical treatment on how to handle the variable viscosity term is described in more detail in [42,10] so we omit here. Fig. 10 shows the vesicle tumbling motion with the reduced volume $\nu = 0.8$ and the dimensionless shear rate $\chi = 100$ up to the same time $t = 24$ as the TT motion. One might wonder whether the volume leakage becomes severe when the vesicle tumbles for long time simulations. To the best of our experience, in addition to have sufficiently large number of triangles to represent the vesicle surface, one can add a volume conservation penalty term to the right-hand side of Eq. (25) to have better volume preservation. This extra volume conservation penalty term has the form as

$$\mathbf{F}_v \, dA(\mathbf{X}) = -C_v \left(\frac{V^t - V^0}{V^0} \right) \mathbf{n} \, dA(\mathbf{X}), \tag{30}$$
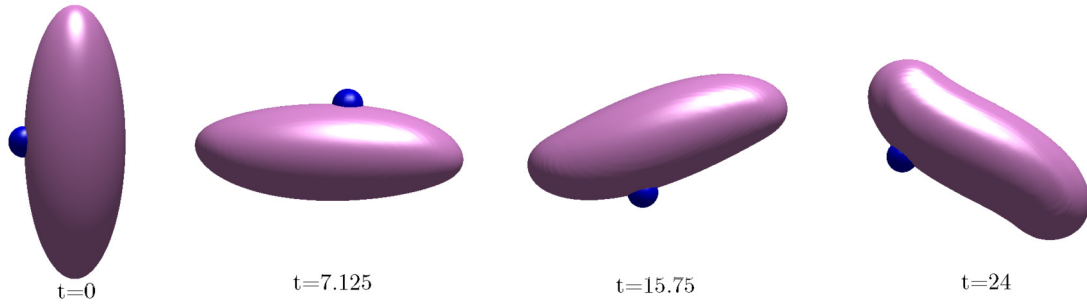
Fig. 10. Tumbling motion of a vesicle with $\nu = 0.8$ and $\lambda = 40$ in a shear flow with $\chi = 100$. The computed time is up to $t = 24$.
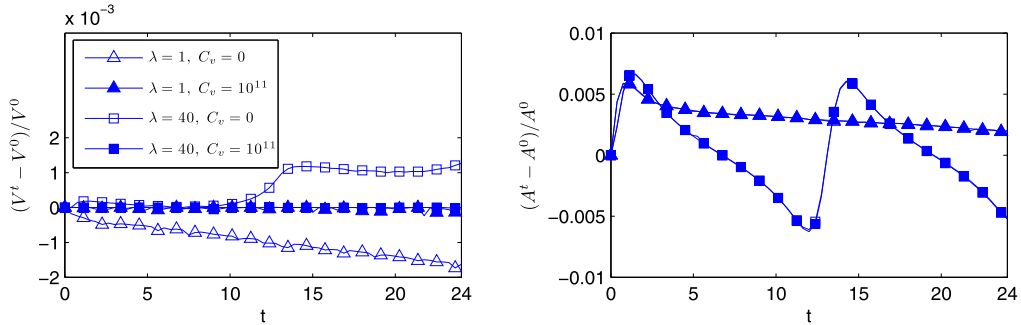
Fig. 11. The volume relative errors (left) and the surface area relative errors (right) for the cases of with or without the penalty volume conservation term Eq. (30). Here, $\nu = 0.8$ and $\chi = 100$. The viscosity contrast $\lambda = 1$ and $\lambda = 40$, respectively.

where C_v is a sufficiently large penalty constant, V^t is the computed volume of vesicle at time t, and V^0 is the total volume of initial vesicle. Note that, this volume preservation remedy has been implemented in the framework of front-tracking method in literature such as in [48]. In the left panel of Fig. 11, we show the volume relative error comparisons with or without addition of Eq. (30) for the cases of $\lambda = 1$ and $\lambda = 40$, respectively. Here, we choose the penalty constant $C_v = 10^{11}$. As you can see from the figure, by adding the force term of Eq. (30), the volume relative error keeps steady while without adding the force term, the volume relative error will slightly change as time goes (still within 0.2% up to $t = 24$). More importantly, by adding this volume conservation penalty term, the vesicle surface area will not be affected as you can see both surface area relative errors are coincided with each other in the right panel of Fig. 11. It is also interesting to see that the surface area relative error for the tumbling case $\lambda = 40$ oscillates more apparently than the tank-treading case $\lambda = 1$. Although it is not shown here, the vesicle dynamics remain the same whether the force term of Eq. (30) is added or not. Therefore, for long time vesicle simulations, it is recommended to add the volume conservation penalty term in Eq. (25).

4.6. A vesicle under the gravity

As in [3,45], we study the shape deformation under gravitational effect by considering different fluid density across the vesicle boundary. To simulate this problem, we simply add an interfacial force $\mathbf{F}_g \mathrm{d}A(\mathbf{X}) = (\rho^i - \rho^e)(\mathbf{g} \cdot \mathbf{X}) \mathrm{d}A(\mathbf{X}) \mathbf{n}$ into Eq. (25) where ρ^i and ρ^e are interior and exterior fluid densities, respectively, and $\mathbf{g} = (0, 0, -1)$ is the dimensionless gravitational field. Here, we consider two different initial shapes (prolate and oblate) of vesicle described by

- $\mathbf{X}(\theta, \phi) = (0.5 \cos\theta \sin\phi, 0.5 \sin\theta \sin\phi, \cos\phi)$,
- $\mathbf{X}(\theta, \phi) = (0.75 \cos\theta \sin\phi, 0.75 \sin\theta \sin\phi, 0.375 \cos\phi)$,

which have the reduced volumes $\nu = 0.895$ and $\nu = 0.872$, respectively.

The prolate vesicle is placed at different tilted angles $\eta = 0, \pi/4$ and $\pi/2$ initially to see how the initial orientation affects the equilibrium shape. A few snapshots up to equilibrium for the prolate vesicle with the three different tilted angles are shown in the first three columns in Fig. 12. The prolate vesicle with the tilted angle $\eta = 0$ and $\pi/4$ tends to deform into a 'pear-like' shape, whereas the one with the tilted angle $\eta = \pi/2$ tends to deform into a 'bean-like' shape. The oblate vesicle shown in the fourth column tends to deform into a 'parachute-like' shape. Although not shown here, the cross-sectional views of the vesicle configurations are pretty similar to those in our previous 3D axisymmetric study [17], indicating that our present vesicle modeling preserves symmetric structure well. Furthermore, the deformations of these vesicles under gravity are in a good agreement with the ones in literature [3,45].
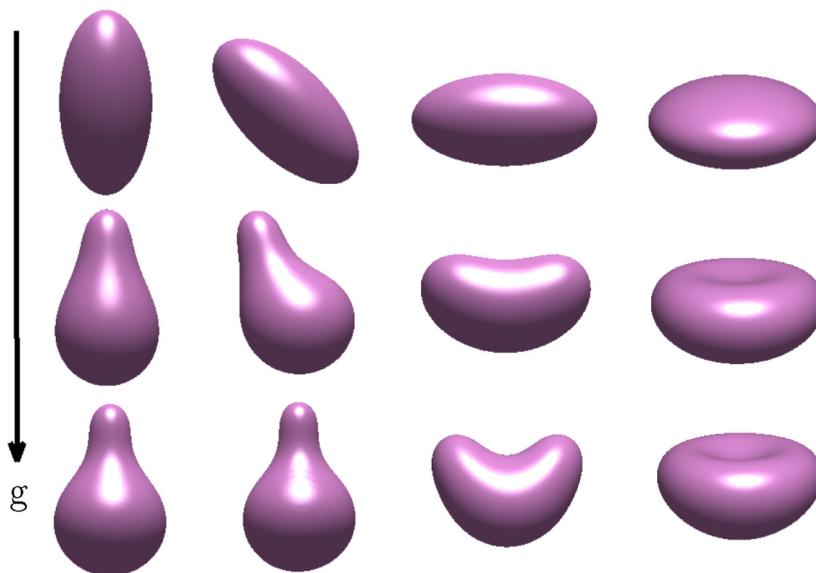
Fig. 12. The prolate vesicle with three different tilted angles $\eta = 0, \pi/4, \pi/2$ (first to third column) and oblate (fourth column) vesicle under the gravity. All the snapshots are taken at the same time.

5. Conclusion and future work

We have proposed an immersed boundary method to simulate the fully three-dimensional vesicle dynamics in various flows. We relax the incompressibility constraint of a vesicle membrane by using a spring-like tension to keep the local surface area nearly incompressible. The new elastic force is derived from a modified tension energy which has exactly the same form as the original one. The vesicle surface is discretized on a triangular mesh, and the elastic tension and bending force are calculated on the vertices of the triangles (Lagrangian markers in the IB method). A series of numerical tests have been conducted to illustrate the robustness and the applicability of the present method.

We have to mention that the nearly incompressible idea for treating the vesicle membrane is not completely new due to different variants existed in literature. For instance, Skalak et al. [38] developed a similar discrete type of strain energy function that involves two local principal stretch ratios on the surface patch with a sufficiently large energy constant to ensure the resistance against area dilation in red blood cell membrane. Yazdani & Bagchi [48] applied the above strain energy function to each triangular element of the vesicle surface and derived the in-plane (tangential) force based on the discrete principle of virtual work. Although our present modified elastic tension energy in Eq. (14) and the above strain energy are similar in spirit, as mentioned in Section 2.1, the present derived elastic force matches the same mathematical form as shown in Eq. (7) and has both tangential and normal components while the latter force derived from the strain energy remains tangential only. Meanwhile, the present nearly incompressible approach might have some limitations in applications to more general 3D vesicle simulations such as the study of vesicle trembling under shear flow. We will leave this investigation to future work.

In the future, we shall also try to use high-order scheme [4] to compute the geometrical quantities such as mean curvature and surface Laplacian of mean curvature on a triangulated surface so that the numerical accuracy for the elastic and bending forces on a vesicle can be further improved. Meanwhile, we shall use the developed scheme to study the vesicle dynamics in more general flows such as in extensional flow [23] or in Poiseuille flow [5]. In the latter case, we will also study the multi-vesicle problems to mimic the physical behaviors of RBCs in capillary [39].

Acknowledgements

Appendix A

In this appendix, we shall show that our formula for the mean curvature vector at vertex **X** as shown in Eq. (21) is exactly the same as the following cotangent formula in [31]
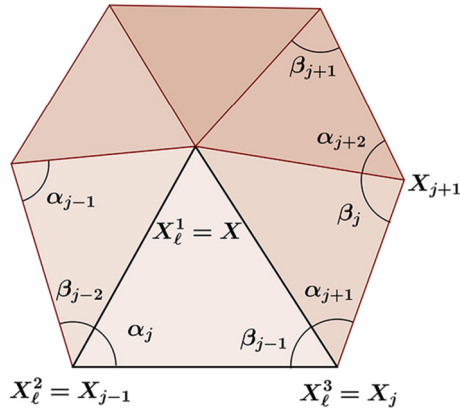
Fig. 13. The notations for the computation of the mean curvature vector using two equivalent formulas.

$$\mathbf{H}(\mathbf{X})\mathrm{d}A(\mathbf{X}) = \frac{1}{2}\sum_{j=1}^{N}\big(\cot\alpha_j + \cot\beta_j\big)(\mathbf{X} - \mathbf{X}_j),\tag{31}$$

where $\mathbf{X}_j$ are the vertices within 1-ring of the vertex $\mathbf{X}$, and the angles α_j and β_j are the corresponding angles depicted in Fig. 13. First we can change the right-hand side of Eq. (31) into the following:

$$\frac{1}{2}\sum_{j=1}^{N}\big(\cot\alpha_j + \cot\beta_j\big)(\mathbf{X} - \mathbf{X}_j)$$

$$= -\frac{1}{2}\sum_{j=1}^{N}\cot\alpha_j(\mathbf{X}_j - \mathbf{X}) + \cot\beta_j(\mathbf{X}_j - \mathbf{X})$$

$$= -\frac{1}{2}\sum_{j=1}^{N}\cot\alpha_j(\mathbf{X}_j - \mathbf{X}) + \cot\beta_{j-1}(\mathbf{X}_{j-1} - \mathbf{X})\ \ \text{(using the periodicity of index)}$$

$$= -\frac{1}{2}\sum_{j=1}^{N}\cot\alpha_j(\mathbf{X}_\ell^3 - \mathbf{X}_\ell^1) + \cot\beta_{j-1}(\mathbf{X}_\ell^2 - \mathbf{X}_\ell^1)\ \ \text{(denoting the vertices in the }\ell\text{-th triangle)}$$

$$= -\frac{1}{2}\sum_{j=1}^{N}\cot\alpha_j\mathbf{X}_{31} + \cot\beta_{j-1}\mathbf{X}_{21}\ \ \text{(where }\mathbf{X}_{ij} = \mathbf{X}_\ell^i - \mathbf{X}_\ell^j).\tag{32}$$

Using the identity $\cot\theta = \frac{\mathbf{a}\cdot\mathbf{b}}{|\mathbf{a}\times\mathbf{b}|} = \frac{\mathbf{a}\cdot\mathbf{b}}{2\,\mathrm{d}A}$, where θ is the angle between the two vectors $\mathbf{a}$ and $\mathbf{b}$, for the ℓ-th triangle with the vertices $\mathbf{X}_\ell^1$, $\mathbf{X}_\ell^2$, $\mathbf{X}_\ell^3$ and its area $\mathrm{d}A_\ell$, we obtain

$$\cot\alpha_j = \frac{\mathbf{X}_{12}\cdot\mathbf{X}_{32}}{2\,\mathrm{d}A_\ell}, \quad \cot\beta_{j-1} = \frac{\mathbf{X}_{13}\cdot\mathbf{X}_{23}}{2\,\mathrm{d}A_\ell}.$$

Substituting these cotangents into Eq. (32) and summing all the triangles $T(\mathbf{X})$ within 1-ring around the vertex $\mathbf{X}$ as shown in Fig. 13, we have

$$\frac{1}{2}\sum_{\ell\in T(\mathbf{X})}\frac{(\mathbf{X}_{21}\cdot\mathbf{X}_{32})\mathbf{X}_{31} - (\mathbf{X}_{31}\cdot\mathbf{X}_{32})\mathbf{X}_{21}}{2\,\mathrm{d}A_\ell},$$

which, using the vector triple product $(\mathbf{a}\times\mathbf{b})\times\mathbf{c} = (\mathbf{a}\cdot\mathbf{c})\mathbf{b} - (\mathbf{b}\cdot\mathbf{c})\mathbf{a}$, becomes

$$\frac{1}{2}\sum_{\ell\in T(\mathbf{X})}\frac{(\mathbf{X}_{21}\times\mathbf{X}_{31})\times\mathbf{X}_{32}}{2\,\mathrm{d}A_\ell}$$

$$= \frac{1}{2}\sum_{\ell\in T(\mathbf{X})}\frac{(\mathbf{X}_{21}\times\mathbf{X}_{31})\times\mathbf{X}_{32}}{|\mathbf{X}_{21}\times\mathbf{X}_{31}|}$$

$$= \frac{1}{2}\sum_{\ell\in T(\mathbf{X})}\mathbf{n}_\ell\times\mathbf{X}_{32} = \frac{1}{2}\sum_{\ell\in T(\mathbf{X})}\mathbf{n}_\ell\times(\mathbf{X}_\ell^3 - \mathbf{X}_\ell^2).$$

Therefore, we establish the equivalence between the cotangent formula and our formula in Eq. (21) for the computation of the mean curvature vector. Note that, in practice, our formula avoids evaluating the cotangent functions and thus is faster to compute than the cotangent formula.

References

[1] S. Aland, S. Egerer, J. Lowengrub, A. Voigt, Diffuse interface models of locally inextensible vesicles in a viscous fluid, J. Comput. Phys. 277 (2014) 32–47.
[2] T. Biben, K. Kassner, C. Misbah, Phase-field approach to three-dimensional vesicle dynamics, Phys. Rev. E 72 (2005) 041921.
[3] G. Boedec, M. Leonetti, M. Jaeger, 3D vesicle dynamics simulations with a linearly triangulated surface, J. Comput. Phys. 230 (2011) 1020–1034.
[4] S.-G. Chen, M.-H. Chi, J.-Y. Wu, High-order algorithms for Laplace–Beltrami operators and geometric invariants over curved surfaces, J. Sci. Comput. 65 (2015) 839–865.
[5] G. Coupier, A. Farutin, C. Minetti, T. Podgorski, C. Misbah, Shape diagram of vesicles in Poiseuille flow, Phys. Rev. Lett. 108 (2012) 178106.
[6] J. Deschamps, V. Kantsler, E. Segre, V. Steinberg, Dynamics of a vesicle in general flow, Proc. Natl. Acad. Sci. USA 106 (2009) 11444–11447.
[7] M. DoCarmo, Differential Geometry of Curves and Surfaces, Pearson, 2009.
[8] V. Doyeux, V. Chabannes, C. Prud'Homme, M. Ismail, Simulation of vesicle using level set method solved by high order finite element, in: ESAIM Proc., vol. 38, 2012, pp. 335–347.
[9] Q. Du, C. Liu, X. Wang, A phase field approach in the numerical study of the elastic bending energy for vesicle membranes, J. Comput. Phys. 198 (2004) 450–468.
[10] T.G. Fai, B.E. Griffith, Y. Mori, C.S. Peskin, Immersed boundary method for variable viscosity and variable density problems using fast constant-coefficient linear solvers I: numerical method and results, SIAM J. Sci. Comput. 35 (2013) B1132–B1161.
[11] A. Farutin, T. Biben, C. Misbah, Analytical progress in the theory of vesicles under linear flow, Phys. Rev. E 81 (2010) 061904.
[12] A. Farutin, T. Biben, C. Misbah, 3D numerical simulations of vesicle and inextensible capsule dynamics, J. Comput. Phys. 275 (2014) 539–568.
[13] A. Fischer, A. Franco, T. Oberholzer, Giant vesicles as microreactors for enzymatic mRNA synthesis, ChemBioChem 3 (2002) 409–417.
[14] J.L. Guermond, P. Minev, J. Shen, An overview of projection methods for incompressible flows, Comput. Methods Appl. Mech. Eng. 195 (2006) 6011–6045.
[15] F.H. Harlow, J.E. Welsh, Numerical calculation of time-dependent viscous incompressible flow of fluid with a free surface, Phys. Fluids 8 (1965) 2181–2189.
[16] W. Helfrich, Elastic properties of lipid bilayers: theory and possible experiments, Z. Naturforsch., C 28 (1973) 693–703.
[17] W.-F. Hu, Y. Kim, M.-C. Lai, An immersed boundary method for simulating the dynamics of three-dimensional axisymmetric vesicles in Navier–Stokes flows, J. Comput. Phys. 257 (2014) 670–686.
[18] Y. Kim, M.-C. Lai, Simulating the dynamics of inextensible vesicles by the penalty immersed boundary method, J. Comput. Phys. 229 (2010) 4840–4853.
[19] Y. Kim, M.-C. Lai, C.S. Peskin, Y. Seol, Numerical simulations of three-dimensional foam by the immersed boundary method, J. Comput. Phys. 269 (2014) 1–21.
[20] M.-C. Lai, W.-F. Hu, W.-W. Lin, A fractional step immersed boundary method for Stokes flow with an inextensible interface enclosing a solid particle, SIAM J. Sci. Comput. 34 (2012) B692–B710.
[21] Z. Li, M.-C. Lai, New finite difference methods based on IIM for inextensible interfaces in incompressible flows, East Asian J. Appl. Math. 1 (2011) 155–171.
[22] V. Kantsler, V. Steinberg, Orientation and dynamics of a vesicle in tank-treading motion in shear flow, Phys. Rev. Lett. 95 (2005) 258101.
[23] V. Kantsler, E. Segre, V. Steinberg, Vesicle dynamics in time-dependent elongation flow: wrinkling instability, Phys. Rev. Lett. 99 (2007) 178102.
[24] V. Kantsler, E. Segre, V. Steinberg, Critical dynamics of vesicle stretching transition in elongational flow, Phys. Rev. Lett. 101 (2008) 048101.
[25] S.R. Keller, R. Skalak, Motion of a tank-treading ellipsoidal particle in a shear flow, J. Fluid Mech. 120 (1982) 27–47.
[26] M. Kraus, W. Wintz, U. Seifert, R. Lipowsky, Fluid vesicles in shear flow, Phys. Rev. Lett. 77 (1996) 3685–3688.
[27] A. Laadhari, P. Saramito, C. Misbah, Computing the dynamics of biomembranes by combining conservative level set and adaptive finite element methods, J. Comput. Phys. 263 (2014) 328–352.
[28] V.V. Lebedev, K.S. Turitsyn, S.S. Vergeles, Dynamics of nearly spherical vesicles in an external flow, Phys. Rev. Lett. 99 (2007) 218101.
[29] E. Maitre, T. Milcent, G.-H. Cottet, A. Raoult, Y. Usson, Applications of level set methods in computational biophysics, Math. Comput. Model. 49 (2009) 2161–2169.
[30] E. Maitre, C. Misbah, P. Peyla, A. Raoult, Comparison between advected-field and level-set methods in the study of vesicle dynamics, Physica D 241 (2012) 1146–1157.
[31] M. Meyer, M. Desbrun, P. Schröder, A.H. Barr, Discrete differential-geometry operators for triangulated 2-manifolds, in: H.-C. Hege, K. Polthier (Eds.), Visualization and Mathematics III, Springer, Berlin, 2003, pp. 35–57.
[32] C. Misbah, Vacillating breathing and tumbling of fluid vesicles under shear flow, Phys. Rev. Lett. 96 (2006) 028104.
[33] H. Noguchi, G. Gompper, Shape transitions of fluid vesicles and red blood cells in capillary flows, Proc. Natl. Acad. Sci. USA 102 (2005) 14159–14164.
[34] H. Noguchi, G. Gompper, Swinging and tumbling of fluid vesicles in shear flow, Phys. Rev. Lett. 98 (2007) 128103.
[35] C.S. Peskin, The immersed boundary method, Acta Numer. 11 (2002) 479–517.
[36] J.M. Rallison, A. Acrivos, A numerical study of the deformation and burst of a viscous drop in an extensional flow, J. Fluid Mech. 89 (1978) 191–200.
[37] D. Salac, M. Miksis, A level set projection model of lipid vesicles in general flows, J. Comput. Phys. 230 (2011) 8192–8215.
[38] R. Skalak, A. Tozeren, R.P. Zarda, S. Chien, Strain energy function of red blood cell membranes, Biophys. J. 13 (1973) 245–264.
[39] L. Shi, T.-W. Pan, R. Glowinski, Three-dimensional numerical simulation of red blood cell motion in Poiseuille flows, Int. J. Numer. Methods Fluids 76 (2014) 397–415.
[40] S. Sofou, Surface-active liposomes for targeted cancer therapy, Nanomedicine 2 (2007) 711–724.
[41] Z. Tan, Duc-Vinh Le, K.M. Lim, B.C. Khoo, An immersed interface method for the simulation of inextensible interfaces in viscous fluids, Commun. Comput. Phys. 11 (2012) 925–950.
[42] G. Tryggvason, R. Scardovelli, S. Zaleski, Direct Numerical Simulations of Gas–Liquid Multiphase Flows, Cambridge University Press, 2011.
[43] S.K. Veerapaneni, D. Gueyffier, D. Zorin, G. Biros, A boundary integral method for simulating the dynamics of inextensible vesicles suspended in a viscous fluid in 2D, J. Comput. Phys. 228 (2009) 2334–2353.
[44] S.K. Veerapaneni, D. Gueyffier, D. Zorin, G. Biros, A numerical method for simulating the dynamics of 3D axisymmetric vesicles suspended in viscous flows, J. Comput. Phys. 228 (2009) 7233–7249.
[45] S.K. Veerapaneni, A. Rahimian, G. Biros, D. Zorin, A fast algorithm for simulating vesicle flows in three dimensions, J. Comput. Phys. 230 (2011) 5610–5634.
[46] J.L. Weiner, On a problem of Chen, Willmore et al., Indiana Univ. Math. J. 27 (1978) 19–35.
[47] C.-H. Wu, T.G. Fai, P.J. Atzberger, C.S. Peskin, Simulation of osmotic swelling by the stochastic immersed boundary method, preprint.
[48] A. Yazdani, P. Bagchi, Three-dimensional numerical simulation of vesicle dynamics using a front-tracking method, Phys. Rev. E 85 (2012) 056308.

[49] N.J. Zabusky, E. Segre, J. Deschamps, V. Kantsler, V. Steinberg, Dynamics of vesicles in shear and rotational flows: modal dynamics and phase diagram, Phys. Fluids 23 (2011) 041905.
[50] H. Zhao, E.S.G. Shaqfeh, The dynamics of a vesicle in simple shear flow, J. Fluid Mech. 674 (2011) 578–604.
[51] H. Zhou, C. Pozrikidis, Deformation of liquid capsules with incompressible interfaces in simple shear flow, J. Fluid Mech. 283 (1995) 175–200.